



Highly selective regeneration of 1,4-NADH enabled by a metal-free core-shell photocatalyst of resorcinol-formaldehyde resins@polyaniline under visible light

Liang Zhou^{a,b,c,d}, Zheng Su^{a,b,d}, Jia Wang^{a,b,d}, Yannan Cai^a, Ningkai Ding^a, Lingzhi Wang^{d,e}, Jinlong Zhang^{d,e}, Yongdi Liu^{a,b,d}, Juying Lei^{a,b,c,d,*}

^a National Engineering Research Center of Industrial Wastewater Detoxication and Resource Recovery, East China University of Science and Technology, 130 Meilong Road, Shanghai 200237, PR China

^b State Environmental Protection Key Laboratory of Environmental Risk Assessment and Control on Chemical Process, East China University of Science and Technology, 130 Meilong Road, Shanghai 200237, PR China

^c Shanghai Institute of Pollution Control and Ecological Security, Shanghai 200092, PR China

^d Shanghai Engineering Research Center for Multi-media Environmental Catalysis and Resource Utilization, East China University of Science and Technology, 130 Meilong Road, Shanghai 200237, PR China

^e Key Laboratory for Advanced Materials and Joint International Research Laboratory of Precision Chemistry and Molecular Engineering, Feringa Nobel Prize Scientist Joint Research Center, School of Chemistry and Molecular Engineering, East China University of Science and Technology, 130 Meilong Road, Shanghai 200237, PR China

ARTICLE INFO

Keywords:

Photocatalyst

Metal-free

Resorcinol-formaldehyde resins

NADH

Regeneration

ABSTRACT

Cofactors, including reduced nicotinamide adenine dinucleotide (NADH), are involved in approximately 80 % of oxidoreductase-catalyzed reactions. However, NADH has not been widely used in the industrial production processes due to cost factors. In this work, we have designed a kind of metal-free core-shell photocatalyst with resorcinol-formaldehyde resin spheres as the core and polyaniline as the shell (RF@PANI) for the highly efficient and selective photocatalytic regeneration of 1,4-NADH (only 1,4-NADH has enzyme activity). It was demonstrated that the introduction of the carbonyl group and the sum of electronic effects made the C4 site of NAD⁺ a more electrophilic hydride transfer site rather than C6 and C2 in the RF@PANI system, leading to the high selectivity of NAD⁺ to 1,4-NADH. The discovery of this mechanism will guide the design of more efficient and highly selective catalysts to break through the cost limitations for the large-scale applications of NADH.

1. Introduction

At present, clean energy technologies such as enzyme-catalyzed reductions and hydrogenation of high-valence carbon molecules into methane have attracted widespread attention [1–4]. This kind of redox enzymatic reaction can efficiently reduce carbonyl, carboxyl, and carbon-carbon double bonds, in which cofactors are mostly consumed [5–7]. It is reported that 80 % of such reactions require the coenzyme NADH as the hydrogen source. In the its enzymatically active form of 1, 4-NADH, the molecule transfers two electrons and a proton to a substrate in the presence of a suitable enzyme, resulting in the oxidation of NADH to NAD⁺. The cost per mole of NADH is as high as US \$2600 per mole, and the continuous addition of NADH greatly increases the cost of the process. Therefore, the efficient regeneration of NADH is of

particular interest for both academic and industrial applications [8]. Among various regeneration technologies, the photocatalytic NADH regeneration provides a nonconventional and green approach to utilizing solar energy for advanced biomanufacturing [9–11].

Up until now, various photocatalysts with high conversion efficiency of NAD⁺ to NADH have been reported. For example, a metal-organic framework (MOF) MIL-125-NH₂ photocatalyst can regenerate NADH with a yield of 66.4 % in 60 min. TiO₂-CdS nanotubes achieved a 75.2 % regeneration yield within 120 min [12]. Similarly, an 80 % NADH regeneration yield was obtained within 1 h by using CdS-coated SiO₂ beads as the photocatalyst [13]. A rationally designed olefin-linked covalent organic framework (COF) incorporated with Cp*Rh(H₂O) can be effective for NADH regeneration accumulated up to 80 % yield within 20 min [14]. However, little attention has been paid to the selectivity of

* Corresponding author at: National Engineering Research Center of Industrial Wastewater Detoxication and Resource Recovery, East China University of Science and Technology, 130 Meilong Road, Shanghai 200237, PR China.

E-mail address: leijuying@ecust.edu.cn (J. Lei).

<https://doi.org/10.1016/j.apcatb.2023.123290>

Received 7 July 2023; Received in revised form 25 August 2023; Accepted 14 September 2023

Available online 17 September 2023

0926-3373/© 2023 Elsevier B.V. All rights reserved.

photocatalytic conversion of NAD^+ to the enzymatically active 1,4-NADH while the inactive products 1,2-NADH, 1,6-NADH, NAD dimers, and deep hydrogenation products are always accompanied during the reduction conversion process [15]. It was reported that the electron mediator (EM), a rhodium-based compound $(\text{Cp}^*\text{Rh}(\text{bpy})(\text{H}_2\text{O})_2)^{2+}$ which is usually added to the reaction system, can transfer electrons and proton hydrogen to NAD^+ and selectively regenerate 1,4-NADH [16–18]. Obviously, it is also uneconomical to use expensive EM in large quantities. Moreover, there has been no study conducted on improving the selectivity by regulating the properties of the photocatalysts such as their composition and structure. The unselective nature of the photocatalysts and the typically indiscriminate NAD^+ conversion products will hinder the further development of photocatalysis for NADH regeneration.

Meanwhile, in various photocatalytic schemes for NADH generation, the usage of metals has generally been recognized as effective. Precious metals such as Au and Pt, as electron defect centers can efficiently transfer electrons to achieve the efficient regeneration of NADH [19–21]. However, the cost of using precious metals is high and the preparation of materials is cumbersome and unsatisfactory. Some transition metal hybrids have also been reported for photocatalytic regeneration of NADH with good efficiency. However, the leaching of heavy metals may cause secondary pollution, which may be harmful to the enzymatic reactions and the human body, affecting the practical applications [22–24]. Therefore, efficient metal-free photocatalysts are desirable for the photocatalytic regeneration of NADH. Currently, metal-free photocatalysts such as modified carbon nitride and COFs have been explored, but more metal-free photocatalysts with high efficiency for the regeneration of NADH are expected. Our recent work found that the resorcinol-formaldehyde phenolic resin is a potential metal-free catalyst for photocatalytic NADH generation. Recently, polyaniline (PANI) as a kind of p-type organic semiconductor polymer and surface coating material has been widely used catalysts in improving photocatalytic performance [25–28]. Its unique lowest unoccupied molecular orbital (LUMO) and highest unoccupied molecular orbital (HOMO) structures can create heterojunctions and improve the separation efficiency of photo-generated electrons and holes (e^-h^+). In addition, the special flexibility of polyaniline makes it one of the best candidates for the preparation of thin-film core-shell structures [29,30]. Moreover, its superconductivity helps to accelerate the transfer of electrons, and many benzenes ring structures and amino groups are conducive to strengthening π - π conjugation and stacking effects [31].

Herein, a type of metal-free core-shell photocatalytic material was designed and prepared by photo-deposition method for highly selective regeneration of 1,4-NADH, which is composed of resorcinol-formaldehyde phenolic resin as the core and surface-grafted polyaniline as the shell (RF@PANI). The resorcinol-formaldehyde phenolic resin (RF) core and the polyaniline (PANI) shell form a type II heterojunction, which efficiently separates the photo-generated electrons and holes, accelerates electron transfer, and utilizes charge adsorption and π - π group conjugation for NADH regeneration effects at pH 9–10. The obtained catalyst achieved a high yield of 68.0 % (about $620 \mu\text{mol}\cdot\text{g}^{-1}\cdot\text{h}^{-1}$), and the selectivity for regeneration of 1,4-NADH was up to 70.3 %, which is four times higher than pure RF. The mild metal-free material was biologically non-toxic, and demonstrated to be suitable for a wide range of temperature conditions (30–50 °C). Also, it exhibited good repeatability. More importantly, the induction of the carbonyl group and the sum of electronic effects makes the C4 site as a more electrophilic hydride transfer site than C6 and C2 in the RF@PANI system, leading to high selectivity for the directional photocatalytic regeneration of 1,4-NADH. The unique strategy that enhances the selectivity through an amide bond ligand provides new ideas for the development of cost-effective photocatalytic regeneration of NADH.

2. Experimental section

2.1. Synthesis of RF

Resorcinol-formaldehyde resin (RFs) was prepared by a one-pot hydrothermal method. Particularly, a solution containing ethanol (10 mL) and water (40 mL) was mixed with resorcinol and formaldehyde with a mole ratio of 1:2 molar ratio and the mixture was stirred for 30 min. 0.4 g of resorcinol was immersed and intensely stirred in a formaldehyde solution (the solution containing 0.6 mL of formaldehyde, 10 mL of ethanol and 40 mL of deionized water) for 30 min. Subsequently, 0.1 mL of $\text{NH}_3\cdot\text{H}_2\text{O}$ (28 wt %) was slowly added (drop by drop), and the colloidal suspension was further stirred for another 24 h under 313 K. RF was obtained by washing with ethanol and water for several times, followed by drying in a vacuum.

2.2. Synthesis of RF@PANI

The RF@PANI was prepared by the photo-deposition method. Briefly, 250 mg of RF was immersed and dispersed in the mixture, which contained 20 mL of deionized water and 20 mL of ethanol, the above solution was labelled as solution A. At the same time, 2.5 (or 5, 12.5) mg of polyaniline (PANI) was dispersed in 10 mL of deionized water and labeled as solution B. Then the solution B was added to solution A and stirred for 10 min in a quartz tube. After that, the quartz tube was irradiated for 2 h by a 300 W Xe lamp, and the final powder samples were obtained after washing with ethanol and water followed by being dried in a vacuum oven. The resultant samples were denoted as RF@PANI-1, RF@PANI-2 and RF@PANI-5 respectively according to the added amount of PANI. The physically mixed RF+PANI was prepared by mixing the above-mentioned pure RF (250 mg) and PANI (5 mg) which were of same quality as RF@PANI-2.

2.3. Synthesis of the electron mediator (EM)

The EM was prepared using a general method [32]. First of all, 0.4 mmol of $\text{RhCl}_3\cdot 3\text{H}_2\text{O}$ and 0.4 mmol of 1,2,3,4,5-Pentamethylcyclopentadiene were added to 20 mL of methanol, and the mixture was refluxed for 12 h at room temperature to obtain a red precipitate. Secondly, the solution was mixed with 0.8 mmol of 2,2'-Bipyridine and stirred for 1 h to obtain an orange solution, which is evaporated naturally to about 3 mL in a fume hood. Then 10 mL of ether was added for the solid separation due to the difference in polarity. After air-drying at room temperature for several hours, the orange solid of $(\text{Cp}^*\text{Rh}(\text{bpy}))\text{Cl}$ was obtained. Then it was collected to be used in the NADH reaction solution at a concentration of 0.75 mM.

2.4. Photocatalytic NADH regeneration

The reaction solution was composed of EM (0.75 mM), NAD^+ (1 mM), TEOA (6 v/v %), phosphate buffer (pH=7) and catalyst (50 mg). The solution was irradiated by a 300 W xenon lamp equipped with a 420 nm cut-off filter and kept at room temperature and in the atmosphere. The irradiation density was $1400 \text{ mW}/\text{cm}^2$, measured by Light intensity meter (CEL-NP2000–2(10)A, Beijing China Education Au-light Technology Co., LTD.). 1.5 mL of solution was taken out at regular intervals. After centrifugation and filtration, the concentration of NADH was determined by measuring the absorbance of the filtrate at 340 nm with a UV–vis spectrophotometer.

2.5. Alcohol dehydrogenase (ADH) enzyme-catalyzed reaction

Generally, 1 μL of ADH enzyme (300 U) and 2 mL of 18 wt % formaldehyde solution was added to the above-mentioned NADH regeneration reaction diluent. The ADH enzyme was incubated at 37 °C for a sufficient amount of time in advance, and the mixture was detected

with an ultraviolet-visible spectrophotometer after 15 min of reaction.

The NADH yield was calculated by the following equation:

$$NADH \text{ yield} = \frac{C_{NADH}}{C_{0,NADH}} \quad (1)$$

Where C_{NADH} was calculated according to the slope of the standard curve.

Then the 1,4-NADH selectivity was calculated by the following equation:

$$1,4-NADH \text{ selectivity} = \frac{C_{1,4-NADH}}{C_{NADH}} \quad (2)$$

Among the above, $C_{1,4-NADH}$ was calculated by the decreased absorbance intensity at 340 nm after incubation with the ADH enzyme.

2.6. The calculation of Urbach energy

The Urbach equation was based on Urbach's proposal in 1958 and could be used to calculate the band-tail energy of the intermediate gap state [33].

$$\alpha = \alpha_0 \exp(h\nu/E_u) \quad (3)$$

In this equation, E_u is the Urbach energy, α is the absorption coefficient, h is Planck's constant, and ν is the frequency of light. Therefore, the Urbach energy can be calculated by plotting the reciprocal of the

slope of the curve between $\ln \alpha$ and photon energy.

3. Results and discussion

For the preparation of the core-shell RF@PANI catalysts, firstly, RF with quite good sphericity and uniform size (Fig. S1a, b) was prepared by a one-pot hydrothermal method. Subsequently, PANI was grown uniformly onto the surface of RF by a photo-deposition method. Here we also tried the in-situ polymerization methods such as ice bath, impregnation, and hydrothermal methods, which generally obtained samples with serious agglomeration and the loading of PANI could not be uniformly [34,35]. Finally, inspired by the previous study, a photo-deposition method was employed, and the resultant samples had a uniform loading of PANI and exhibited better catalytic performance [36]. The morphology and microstructure of the RF@PANI materials were explored by the characterization methods of SEM, TEM, and HRTEM et al. It can be seen from Fig. 1a that the RF@PANI-2 maintained a spherical shape. Meanwhile, Fig. 1b and c show that the surface of RF@PANI-2 is rougher than RF, and PANI is grown uniformly on the surface of RF. After increasing the loading amount of PANI, a clear and more uniform core-shell structure can be observed by RF@PANI-5 in Figs. S2c and 2d. The thickness of the PANI-shell was about 10 ± 5 and 30 ± 10 nm for RF@PANI-2 and RF@PANI-5. Due to the low content of PANI in RF@PANI-1, the PANI-shell could not be measured accurately (Figs. S2a and 2b). Fig. 1d-e shows the high-resolution image of the

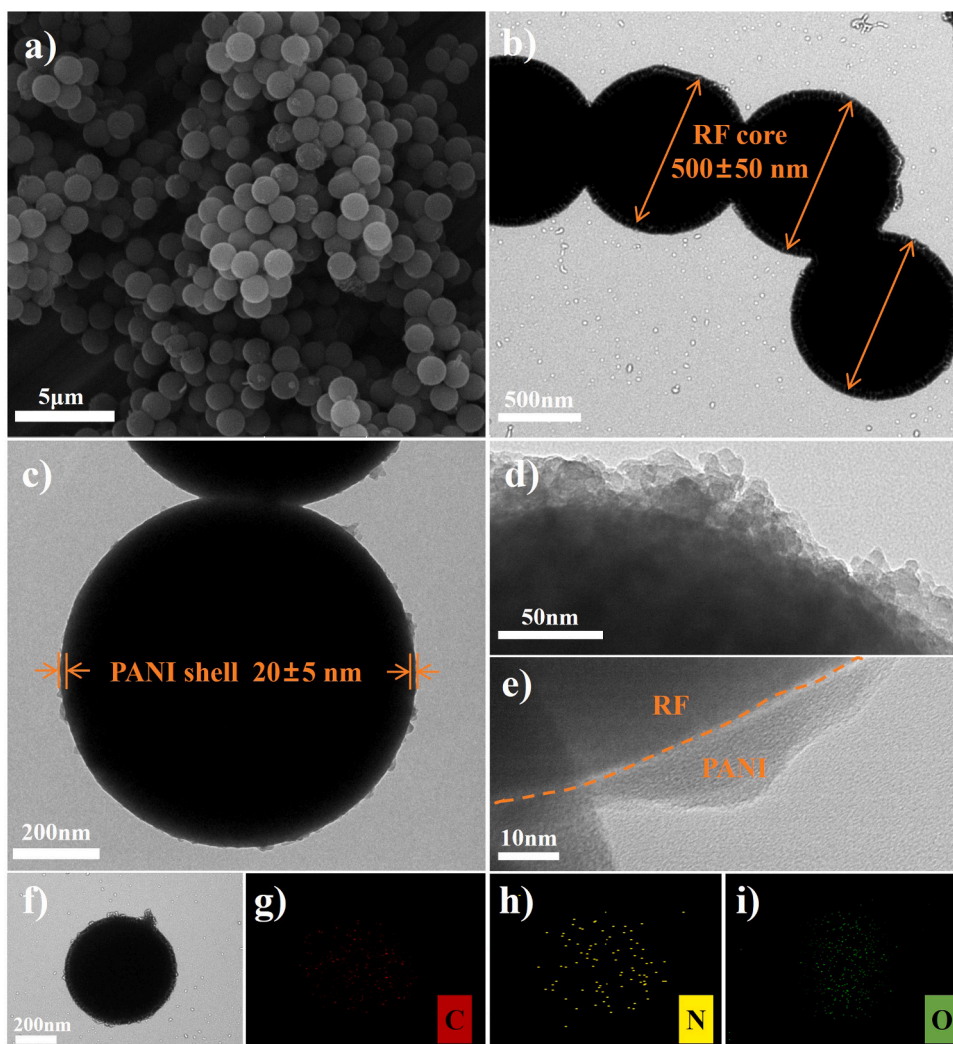


Fig. 1. (a) SEM image, (b-c) TEM images, and (d-e) HRTEM images of RF@PANI-2; (f-i) element mapping images of RF@PANI-2: including elements of C, N, and O.

interface for the core-shell structure of RF@PANI-2. The boundary is clear, which indicates that RF nanospheres remained intact. Furthermore, the element mapping images suggest a uniform distribution of PANI (Fig. 1f-i), confirming the presence of carbon, nitrogen, and oxygen.

The chemical structure of the material was characterized by FT-IR, XPS, et al. The FT-IR spectrum is shown in Fig. 2a. For RF, the broad peak at around 3300 cm^{-1} was attributed to O-H of resorcinol, and the peak at 2925 cm^{-1} belonged to the C-H of methylene linker. The bands around 1700 cm^{-1} and 1620 cm^{-1} were the C=O bending mode of aldehyde residue and quinone unit [37]. Other peaks can be assigned to the C-H of methylene linker at 1450 cm^{-1} , C-H of the aromatic ring at 1370 cm^{-1} , and C-O of resorcinol and methylal at 1240 and 1100 cm^{-1} . After loading PANI, the absorption peak detected at 1600 cm^{-1} belong to C=N stretching, 1500 cm^{-1} of C=C stretching, the peak at 1300 cm^{-1} is assigned to C-N stretching owing to the quinonoid unit, and C-N stretching of a secondary aromatic amine was at 1120 cm^{-1} . The peaks at 1200 cm^{-1} , 810 cm^{-1} and 609 cm^{-1} were all the characteristic peaks of PANI, suggesting the successful formation of RF@PANI-2 composites. What's more, it is exciting that the intensity changes at 3400 cm^{-1} , representing the enhancement of the charge transfer, are significantly enhanced on RF@PANI-2. The complex structure of RF@PANI-2 disturbed the hydrogen environment and enhanced the tensile strength. In addition, the characteristic peak signal similar to PANI at 1500 cm^{-1} was widely considered to be a measure of the electron delocalization degree [38]. Due to the interaction between PANI and RF, the signal intensity of RF@PANI-2 at 1500 cm^{-1} was weaker than at 1600 cm^{-1} . Hence, it can be speculated that the quinoid structure promoted the stability of the D-A conjugate pairs, which further promoted the performance of the catalyst.

To understand the valence state change on the surface of RF@PANI-2, XPS analysis was used to characterize C 1s, O 1s, and N1s orbit scans, as shown in Fig. 2b, c and S3. The binding energy peaks at 284.6, 286.2, 288.0, and 291.0 eV of C 1s confirm that carbon is mainly present in C=C, C-O, C=O, and $\pi\text{-}\pi^*$ conjugation. The $\pi\text{-}\pi^*$ conjugated group was

obviously shifted to low binding energy in RF@PANI-2 due to the strong attraction effect from PANI, which is beneficial to structural stability. The O 1s orbital peaks at 531.4, 532.1, and 533.0 eV could be fitted to C=O, O=C-O, and C-O, respectively. Due to the strong interaction between RF and PANI enhancing the quinoid structure in D-A couples, the ratio of C=O species in RF@PANI-2 was significantly higher than in RF. The deconvolution of the N 1s signal at 398.9, 400.7, and 401.7 eV confirms the characteristic formation of conductive PANI, which is attributed to -N=, -N-, -NH⁺- [29]. The existence of a high ratio of -NH-binding energy indicates that the -NH- of PANI structure strengthened [39]. The RF tested by XRD in Fig. S4 has a strong broad diffraction peak observed at $2\theta \sim 23.3^\circ$, which was attributed to the (002) plane of graphitic carbon, indicating that there was a $\pi\text{-}\pi^*$ stacked aromatic structure in the RF. The existence of this diffraction peak proved that the distance between the aromatic hydrocarbon planes was relatively narrow. It was owing to the strong formation of the quinoid structure as the electron acceptor, through the $\pi\text{-}\pi^*$ stacking interaction of the electron (D-A) pairs with the benzene structure as the electron donor. The PANI material shows a diffraction peak at $2\theta \sim 25.1^\circ$, which is due to the repeating unit of the PANI chains. In RF@PANI-2, the broad diffraction peaks of RF showed a blue shift at $2\theta \sim 21.7^\circ$, indicating the further enhancement of $\pi\text{-}\pi^*$ conjugation and stacking after PANI combined with RF. The absence of PANI peaks might be caused by too little PANI loading on the RF surface. The EDS analysis (Fig. S5), expounds that RF@PANI-2 consists of C, N, and O. The mass fraction ratio of N was 0.20 wt %, which is close to the theoretical content of 0.31 wt %.

The potential light absorption capacity was measured by UV-VIS DRS. As shown in Fig. 3a, RF had strong absorption in the ultraviolet region, and the light absorption edge was around 700 nm. While RF@PANI-2 exhibited wider absorption in the visible light region, which is due to the fact that the polyaniline shell acted as a visible light sensitizer to cause the red shift of absorption edge. Therefore, with the participation of PANI, the increase in the light absorption of RF@PANI-2 could be attributed to the $\pi\text{-}\pi^*$ transition in the benzene and quinone units. As shown in the PL spectra (Fig. S6), compared with RF, the

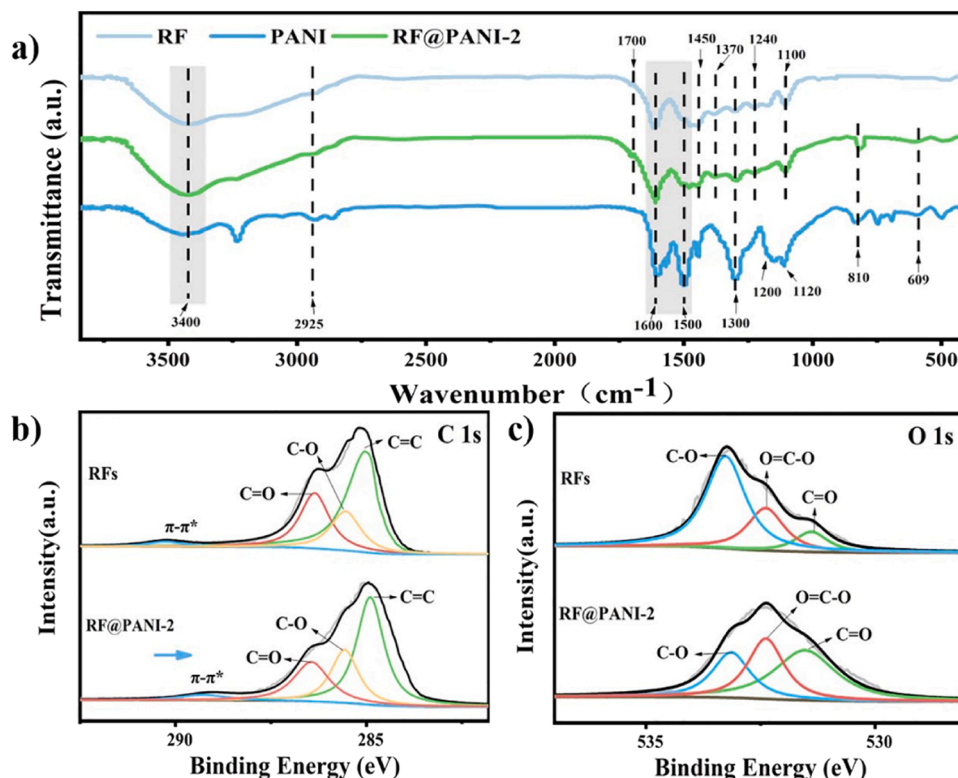


Fig. 2. (a) FT-IR charts of RF, PANI and RF@PANI; High resolution XPS spectra of (b) C 1s, (c) O 1s in RF and RF@PANI-2.

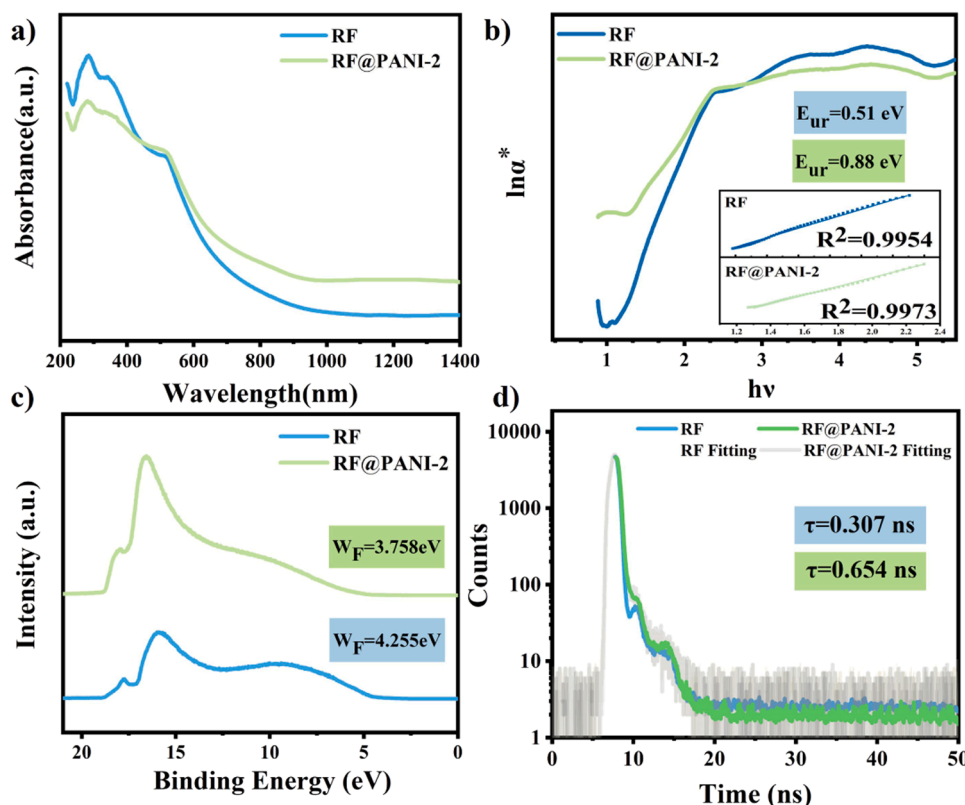


Fig. 3. (a) UV-vis diffuse reflectance spectra of RF, and RF@PANI-2. (b) Urbach energy curves of RF and RF@PANI-2. (c) UPS spectra of RF and RF@PANI-2 for work function. (d) Room temperature ns-level time-resolved PL spectra monitored under 615 nm excitation for RF and RF@PANI-2.

fluorescence signal of RF@PANI-2 is significantly attenuated, indicating that RF@PANI-2 had higher energy and a narrow band gap, which is beneficial to excite more photo-generated electrons. In addition, the spectrum also depicted the extended shoulder-tail transition (Urbach tail) of the RF@PANI sample assigned to the electronic state formed in the band gap, and its energy was applied to describe the disorder extent of the film structure. Fig. 3b shows the respective Urbach plots of RF and RF@PANI-2 (shown as slope fitting in the inset). The E_u of RF@PANI-2 (0.88 eV) was much higher than that of RF (0.51 eV). This thin film with extremely small thickness increased the structural disorder and facilitated the separation of electrons, and the red-shifted energy state is consistent with the former observation of the samples, which could positively affect the light trapping efficiency [15]. In order to demonstrate the improvement effect on the separation of photo-generated electrons from the samples furthermore, the UPS of RF and RF@PANI-2 were tested as shown in Fig. 3c. The work function of RF@PANI-2 was 4.255 eV, and RF@PANI-2 was 3.758 eV. As an N-type semiconductor, the work function of the RF decreased, which means the electrons can escape more easily and promote the migration of charge carriers [40]. Besides, this positive transfer effect is also observed in the photo-electrochemical result. The photocurrent response of the samples (Fig. S7a), clearly shows a higher and enhanced photocurrent response of RF@PANI-2 compared to RF. Similarly, the EIS measurement (Fig. S7b), PANI externalized the smallest semicircular Nyquist diameter due to its superior conductive state performance, followed by RF@PANI-2, and the largest radius was RF, indicating that the charge transfer resistance of RF@PANI-2 was smaller than that of RF. Based on the above discussion, the obtained composite catalyst shows enhanced visible light absorption and efficient separation of the photogenerated charge species, which is beneficial for enhanced photocatalytic performance. Based on high photo-response efficiency and active carrier transfer/migration, the fluorescence lifetime test helped explain the recombination of photo-generated electrons-holes in the bulk phase and

long-distance migration to the surface. As shown in Fig. 3d, after fitting the attenuation spectrum, different fluorescence lifetime could be obtained. Compared with RF, the PANI-composited catalyst shows a longer fluorescence lifetime (Table S1). It was calculated that the total lifetime τ (0.654 ns) of RF@PANI-2 was two times longer than that of RF (0.307 ns). This increment was essential to promote the probability of carriers participating in the reactions. The longer-lived photo-generated electrons and holes have more opportunities to be captured by the reactants, thereby driving more photocatalytic reactions. The zeta potential experiments clarified that RF@PANI-2 had a more negative than RF in alkaline conditions, which is more helpful for the charge to adsorb positively charged NAD^+ and EM, so that electrons transferred to the surface could be efficiently contacted to the active site.

In the photocatalytic NADH regeneration system, its performance was evaluated by utilizing $(Cp^*Rh(bpy)H_2O)^{2+}$ as an electron mediator (EM) and TEOA as a hole scavenger. In the 3-hour reaction (Fig. 4a), all the RF@PANI catalysts showed better catalytic activity. More specifically, the NADH regeneration yield of RF@PANI-1, RF@PANI-2, and RF@PANI-5 can reach 27.17 %, 68.02 % and 37.52 %, which was 1.7, 4.0 and 2.2 times higher than RF, respectively. Fig. 4b shows the results of time-resolved photocatalytic NADH regeneration yield, where the kinetic rate of RF@PANI-2 (about $620 \mu\text{mol}\cdot\text{g}^{-1}\cdot\text{h}^{-1}$) reached the highest in the first 30 min, about five times higher than that of pure RF (about $118 \mu\text{mol}\cdot\text{g}^{-1}\cdot\text{h}^{-1}$), and much higher than that of the physical mixture (RF+PANI) in 3 h. This long-time maintenance of high reaction rate could be attributed to the efficient utilization of sacrificial agent. Therefore, the experiment of photocatalytic NADH regeneration with different amounts of TEOA was carried out and the results are shown in Fig. 4c. The highest yield was obtained with 6 v/v % TEOA, which was lower than the commonly used amount of TEOA, effectively reducing costs. On the other hand, at the same time, it was found that 15 v/v % TEOA could decline the yield of NADH, which might be because too much TEOA could not be completely utilized and would further react

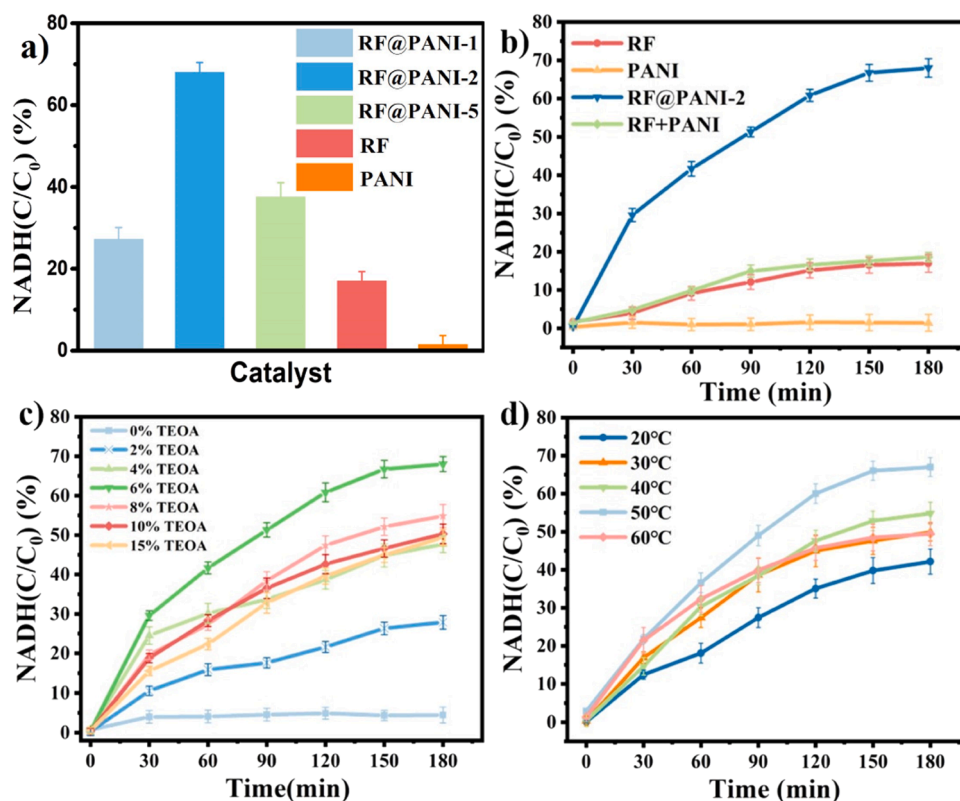


Fig. 4. (a) Photocatalytic NADH regeneration enabled by different catalysts; (b) Time-resolved photocatalytic NADH regeneration yield of different catalysts; (c) Photocatalytic NADH regeneration with the volume fraction of TEOA as a variable with the catalytic RF@PANI-2; (d) Photocatalytic NADH regeneration yield of RF@PANI-2 under different temperature conditions.

with NADH to produce other inactive isomers, or decompose NADH [16]. In practical applications, the appropriate amount of TEOA was the key to saving costs and improving efficiency. What's more, another factor was the temperature of the reaction environment. In the actual enzyme reaction, although too high and too low temperature was not conducive to the progress, it was still possible to fluctuate within a certain range [15,41]. Therefore, it was important to maintain a high NADH yield within a certain range. It could be seen that the activity remained high in the range of 20–50 °C without significantly decreasing. This is because an increase in temperature increases the molecular kinetic energy of the reactant, making it easier for the reactant molecules to overcome the obstacles of activation energy. But for NADH regeneration, excessive temperature will accelerate the decomposition of NADH, ultimately leading to a decrease in the yield of NADH. 20–50 °C has already met the requirements for most enzyme reactions. However, the RF@PANI has shown excellent performance in a wider temperature range, which was conducive to future industrial applications. Likewise, the alkaline pH environment (Fig. S10) is more favorable for the transfer of hydrogen [42]. Therefore, the NAD⁺ conversion rate at pH 10 was significantly higher than that at pH 7. The decrease in the rate with a further increase in pH from 11 results from the deprotonation of the aqua complex (Rh-H₂O) to afford the hydroxo complex (Rh-OH), which may not be active for the heterolysis of hydrogen [43]. The cycle experiment, as shown in Fig. S11a, proved the material had good recycling performance. After four cycles, the NADH yield remained at about 58.32 %. The slight decrease in performance was due to the inevitable loss of the material collection process. Meanwhile, the FTIR of RF@PANI-2 after four cycles of experiments can further confirm the excellent stability of the synthesized catalyst. In Fig. S11b, the peaks belonging to the characteristic structure of the resin were all retained, 1700 cm⁻¹ and 1620 cm⁻¹ for the C=O bending mode of aldehyde residue and quinone unit, 1450 cm⁻¹ for the C-H of methylene linker,

1370 cm⁻¹ for the C-H of aromatic ring, 1240 and 1100 cm⁻¹ for the C-O of resorcinol and methylol. For PANI, the peak at 1200 cm⁻¹, 810 cm⁻¹ and 609 cm⁻¹ was also clearly observed after four cycles. Hence, RF@PANI-2 possesses the property of good chemical stability.

All the above catalytic regeneration of NADH was confirmed by the absorption peak of the UV-Vis spectrum of the reaction solution at 340 nm. In order to further discriminate the regeneration of 1,4-NADH with specific enzyme activity from other inactive substances, the reaction solution of the model catalyst RF@PANI-2 reacted for 3 h under the above optimal conditions was detected by ¹H NMR. As shown in Fig. 5a, compared with the standard samples, characteristic signals of 1,4-NADH and NAD⁺ were observed at 6.87 ppm and 9.28 ppm, respectively. Yet no obvious chemical shift of 1,6-NADH was observed. It was speculated that RF@PANI-2 may have better selectivity for 1,4-NADH regeneration. After prolonging the illumination time to 6 h (Fig. S12), it was observed that the characteristic peak of NAD⁺ disappeared, and the peak of 1,4-NADH was still maintained. The hydrogen transfer caused by the decrease in selectivity and depth hydrogenation in long-term illumination was inevitable. Therefore, it was displayed that the existence of 1,6-NADH (7.02 ppm) and probable NADH attenuation by-products (7.38 ppm) such as NAD₂ dimers and NADH attenuation product. The supplementary explanation was that 1,2-NADH due to its extremely short half-life, was hardly detected stably. Furthermore, alcohol dehydrogenase (ADH) was applied to quantitatively verify the production of 1,4-NADH [44]. As Fig. S13 shows, after enzymatic incubation with ADH enzyme at 37 °C, 1,4-NADH was specifically consumed to make the absorbance at 340 nm decrease. The conversion rate of 1,4-NADH is an important parameter, calculated by substituting the reduced absorbance into the slope as shown in Fig. 5b. It was found that the selectivity of RF@PANI-2 with EM participation for 1,4-NADH regeneration was as high as 70.34 %, while RF was only 38.09 %. In the solution system without EM, it was still observed that the better selectivity of

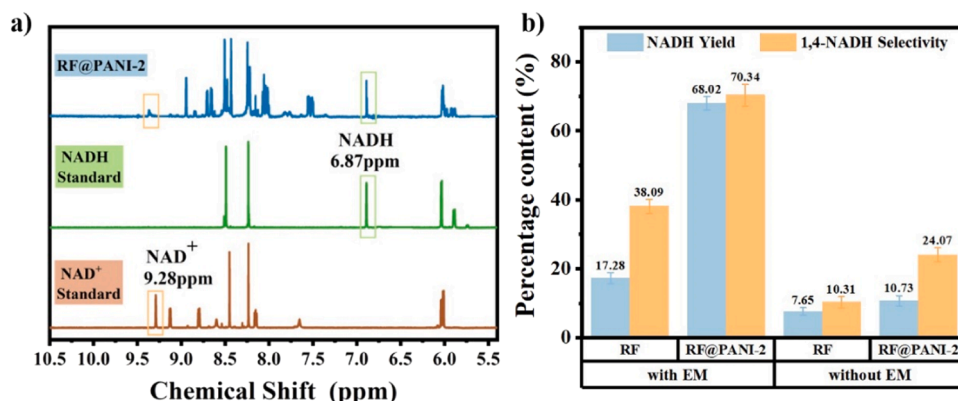


Fig. 5. (a) ^1H NMR spectra of NAD $^+$, NADH, and reaction solution from NAD $^+$ hydrogenation with RF@PANI-2 as the catalyst. (b) NADH yield and 1,4-NADH selectivity of RF and RF@PANI-2 in the system environment with EM or without EM.

RF@PANI-2 (24.07 %) compared with that of RF (10.31 %). The highly selective performance was owing to the complex mechanism of the organic polymer RF@PANI, which promoted the hydrogenation of the C4 site to form the target product.

In order to explore the possible mechanism of photocatalytic regeneration of NADH in RF@PANI, the band gap structure of the resultant catalyst was investigated. Combined with the UV-Vis DRS results, the Kubelka-Munk formula was employed to calculate the band gap energy of the photocatalytic material, the Mott-Schottky curve was applied to determine the conduction band position of the material, and then the valence band position could be calculated. As shown in Fig. S14, the band gap energy of RF was about 2.10 eV, while the

RF@PANI-2 was about 1.95 eV. Through the Mott-Schottky test of different frequencies in Fig. S15, the conduction band bottom of RF was at -0.68 eV, and RF@PANI-2 was at -0.75 eV. Calculated by the formula $E_g = E_{\text{VB}} - E_{\text{CB}}$, the position of the valence band of nanomaterials can be obtained. For RF@PANI-2, the top of the valence band was $+1.2$ eV, and for RF, it was $+1.42$ eV. This also conforms to the general pattern of color change in the sample (Fig. S16). It was worth noting that in Fig. 6a, the position of the conduction band of RF@PANI-2 was more negative as the electron-accepting potential of EM solution (-0.63 eV) and NAD $^+$ /NADH (-0.34 eV), indicating that the photo-generated electrons excited by light can effectively transfer to produce NADH [14,17]. The calculation of the potential structure made the fact that RF@PANI-2 formed a

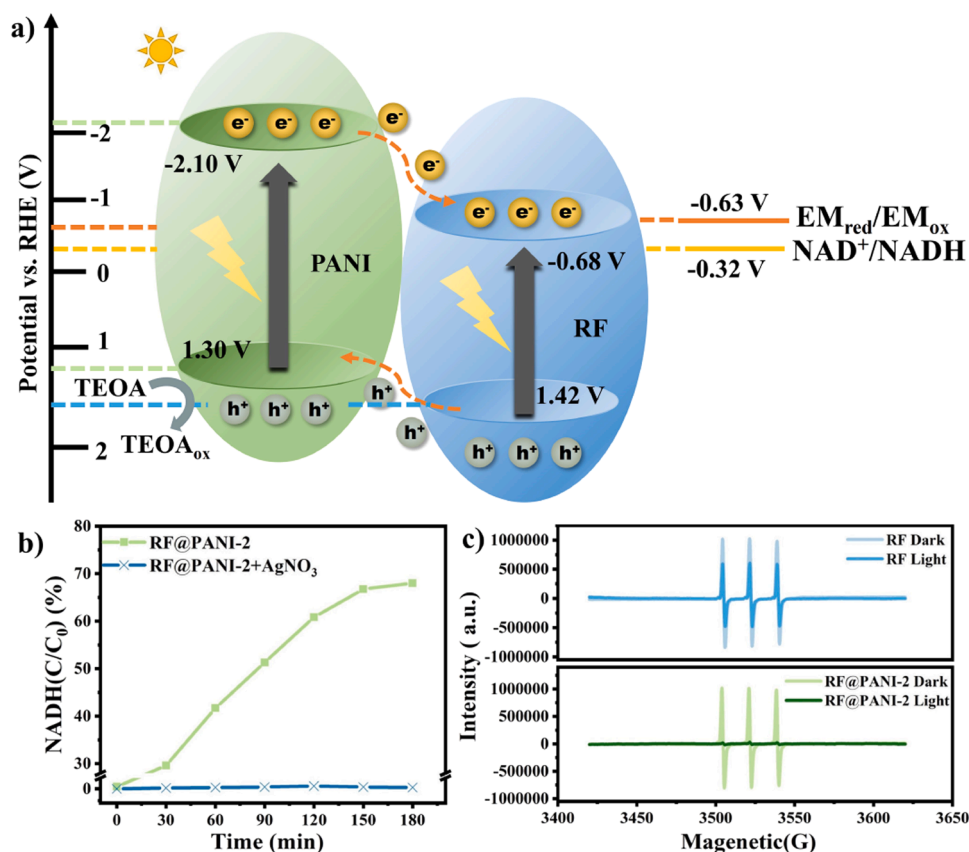


Fig. 6. (a) Illustration of the energy band structure mechanism for NADH regeneration. (b) The influence of photo-generated electron quencher AgNO $_3$ on photocatalytic regeneration of NADH. (c) EPR diagrams of the catalysts RF and RF@PANI-2 to capture photo-generated electrons before and after the light (TEMPO as the capture agent).

type II heterojunction emerges, which can ensure the electrons enrichment at the RF@PANI-2 surface from both RF and PANI, which had demonstrating superior performance for the regeneration of NADH. Meanwhile, the thin thickness of PANI has no significant effect on the diffusion of substrate molecules, the fast mass transfer enables efficient utilization of electrons in heterojunctions [45,46].

What's more, to further explored the photo-generated electrons that played a leading role in the transfer process, quenching and EPR trapping experiments were carried out. As shown in Fig. 6b, when the electron quencher silver nitrate (AgNO_3) was added to the reaction system, the output of NADH was significantly reduced. The results of the EPR in Fig. 6c showed that after the addition of TEMPO to the reaction system, the EPR signals were detected before and after illumination for RF and RF@PANI-2, and it was observed that both two catalysts had the same intensity of triple characteristic peak signals of TEMPO in dark. On the other hand, the triple characteristic peak signal of the RF system after irradiation was weakened, which indicated that RF generated a certain amount of electrons under irradiation. It was conspicuous that after RF@PANI-2 was excited by visible light, the triplet signal of TEMPO dropped significantly. This revealed that RF@PANI-2 generated a large number of photo-generated electrons to be separated and transferred more rapidly than RF, which is consistent with the results of the photoelectric properties. In Fig. S17, by detecting the carbon nuclear magnetic resonance spectrum (^{13}C NMR) of the catalyst, it was observed that the carbon environment of the RF resin structure was similar to the previously reported. RF@PANI-2 did not indicate the formation of a new carbon-related chemical structure, revealing that RF and PANI did not work with carbon as a connecting unit. Combining the XPS N1s (Fig. S3) and FT-IR (Fig. 2a) results, as shown in Fig. 7, on the one hand, there were electron-like absorption structures ($-\text{NH}^+$, $-\text{N} = \text{quinoid}=\text{N}-$) in polyaniline as strong electron-withdrawing effect groups; on the other hand, RF was in addition to the existing benzenoid-quinoid structure as D-A conjugated pairs, for a large number of electronegative hydroxyl groups ($-\text{OH}$) could play the role of electron-donating effect groups, which the combination between RF and PANI owing to inductive effect was extremely reasonable. Utilizing the high conductivity of polyaniline to form an extensible "electron transport chain" that quickly separates electrons, it exerted an ultra-high charge separation effect. Besides, the unique polymer structure of RF and PANI was conducive to the $\pi-\pi^*$ accumulation of the adenine subunit of NAD^+ , combined with the charge adsorption effect to "catch" the reactants on the surface of the catalyst for NADH regeneration. In general, the benzenoid-quinoid unit excited by visible light in the RF structure acted as a D-A conjugated pair to generate electrons and holes, which could be quickly separated through the "electron transport chain" between RF and PANI. After separation, the holes were enriched on the polyaniline and subsequently quenched by TEOA while the electrons were transferred to the RF, and then NADH was regenerated due to the stable binding effect between RF and PANI.

Surprisingly, RF@PANI-2 showed twice as high selectivity as RF for

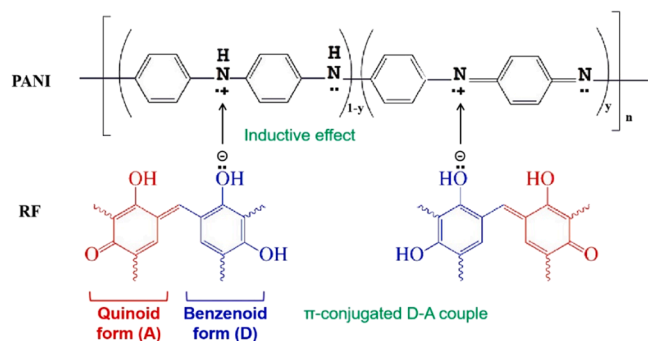


Fig. 7. Fundamental structure of RF and PANI with π -conjugated D-A couple and inductive effect among them.

the selective generation of 1,4-NADH (whether there is M or not). To our knowledge, the mechanism of improving the selectivity of 1,4-NADH by catalyst has not been explored. All the selective reduction of 1,4-NADH is often attributed to the properties of NAD^+ and the characteristics of M. Therefore, we performed in-situ FT-IR detection of RF and RF@PANI-2 under different EM conditions to observe possible surface conditions of the materials. As shown in Fig. 8a, when no EM was added, it could be observed that the RF@PANI-2 has a faster adsorption behavior rate than RF, which weakened the representative peak of NAD^+ at 1650 nm, then generated NADH and released it. While with EM addition in Fig. 8b, for the whole photocatalytic NADH regeneration process, the NADH peak intensity at 1638 nm increased over time, corresponding to the reproductive yield rate of NADH. In photocatalytic reduction reaction, there might be two effective ways for RF@PANI-2 to regenerate 1,4-NADH with high selectivity (Fig. 9). One way was to cooperate with the electronic medium EM, utilizing charge adsorption to regenerate. Two electrons were transferred from the catalyst to $(\text{Cp}^*\text{Rh}(\text{bpy})\text{H}_2\text{O})^{2+}$, and a hydrogen was combined to form $(\text{Cp}^*\text{Rh}(\text{bpy})\text{H})^+$, making the metal Rh as the important binding effect center to coordinate with NAD^+ , which is the potential application way to increase selectivity with EM [17]. The other way was owing to the unique electron-withdrawing structure of PANI, forming the independent role to regenerate 1,4-NADH. In the solution without EM, PANI itself could induce the binding of the amide group of NAD^+ and carry out rapid hydrogen-electron transfer by $\pi-\pi$ conjugation. Combined with the induction of the carbonyl group and the sum of electronic effects, together with the steric hindrance between the functional groups, leading the C4 site as a more electrophilic hydride transfer site than C6 and C2. What's more, the nitrogen atom of the 1-ribosyl moiety on NAD^+ penetrated the electron-withdrawing substituent, which promoted the attack of hydride at the C4 site, causing the result of hydrogenation to generate 1,4-NADH for the reaction. It was believed that these two pathways might have existed at the same time when EM was participated, and the highly selectivity experimental product analysis supported this hypothesis. However, there were still part of the hydrogen at the C4 position due to the electrophilic rearrangement in the molecule to generate C6 and C2, which will reduce the high selectivity to a certain extent. This also explained the decrease in the high selectivity after the prolonged illumination time and then 1,6-NADH and other by-products appeared.

4. Conclusion

In summary, by adjusting the dosage of polyaniline, a series of metal-free organic polymer materials (RF@PANI catalysts) for photocatalytic regeneration of NADH were prepared. Among them, the initial NADH regeneration rate of RF@PANI-2 was more than five times higher than that of RF itself, and the selectivity of 1,4-NADH was as high as 70.3 %. Varieties of characterizations had shown that RF and PANI combined with imine groups and hydroxyl groups due to the induction effect to form a fast "electron transport chain", which helped the D-A conjugate pair to efficiently separate electrons and holes in the benzenoid-quinoid structure of RF. What's more, the chain network promoted polyaniline itself with good conductivity as an electron donor, played a role in synergistic enrichment and transfer of electrons, and combined with the electronic mediator M solution in the highly selective regeneration of 1,4-NADH. In addition, the influence of environmental conditions on the regeneration system was clarified, such as temperature, electronic sacrificial agent, etc. This new metal-free organic polymer design strategy can provide a more enlightening understanding of selective NADH regeneration, and bring new inspiration for the application of joint enzymes to broaden industrialization.

CRedit authorship contribution statement

Liang Zhou: Conceptualization, Investigation, Experiment, Validation, Formal analysis, Writing-original Draft. Zheng Su, Jia Wang,

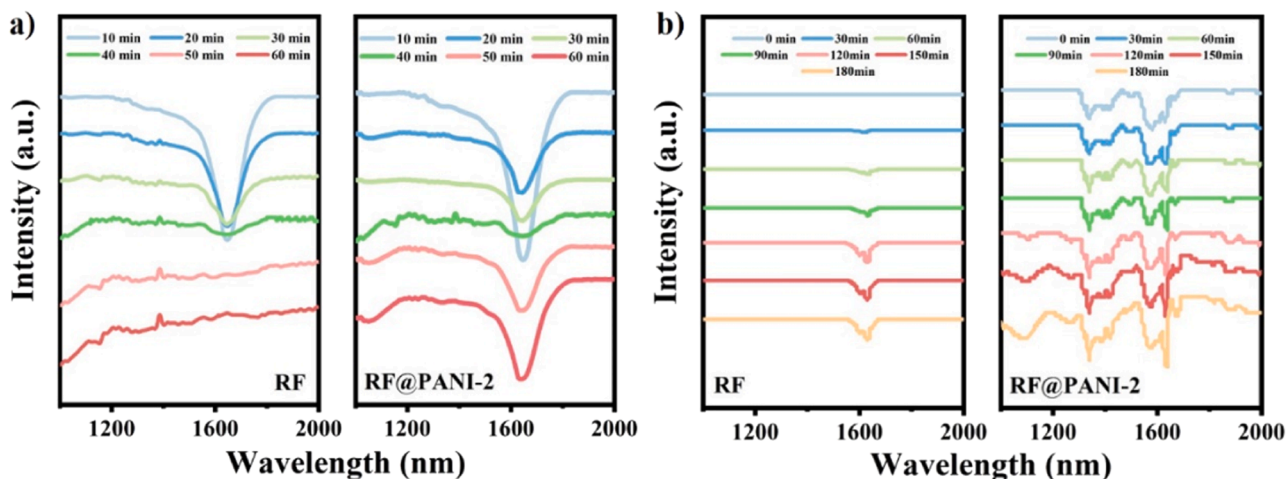


Fig. 8. (a) In-situ FT-IR test about the NAD^+ adsorption on RF and RF@PANI-2 without EM addition. (b) In-situ FT-IR test of the photo-catalysis NADH regeneration process of RF and RF@PANI-2 with EM addition. (The amount of reagents in the regeneration experiments was the same as mentioned before).

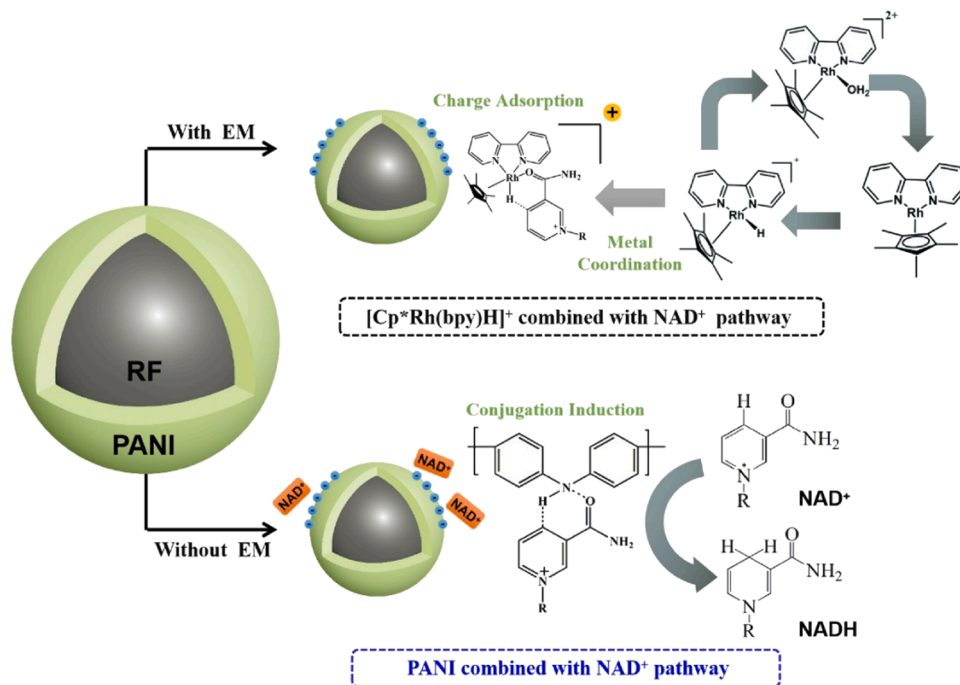


Fig. 9. Illustration of two transfer pathways in RF@PANI and photocatalytic NADH regeneration for specific selection form of 1,4-NADH.

Yannan Cai, Ningkai Ding: Experiment, Formal analysis, Writing-original Draft. Lingzhi Wang, Jinlong Zhang, Yongdi Liu: Conceptualization, Funding acquisition, Project administration, Supervision, Formal analysis, Writing-review & editing. Juying Lei: Conceptualization, Resources, Writing - review & Editing, Supervision, Project administration, Funding acquisition.

Declaration of Competing Interest

The authors declare that they have no known competing financial interests or personal relationships that could have appeared to influence the work reported in this paper.

Data Availability

Data will be made available on request.

Acknowledgments

This work was financially supported by the National Natural Science Foundation of China (22076046, 21777044), the National Key R&D Program of China (2022YFB3803600), and the Fundamental Research Funds for the Central Universities (SLB13233301).

Appendix A. Supporting information

Supplementary data associated with this article can be found in the online version at [doi:10.1016/j.apcatb.2023.123290](https://doi.org/10.1016/j.apcatb.2023.123290).

References

- [1] Z.C. Litman, Y. Wang, H. Zhao, J.F. Hartwig, Cooperative asymmetric reactions combining photocatalysis and enzymatic catalysis, *Nature* 560 (2018) 355–359.

- [2] G. Lin, Y. Zhang, Y. Hua, C. Zhang, C. Jia, D. Ju, C. Yu, P. Li, J. Liu, Bioinspired metalation of the metal-organic framework MIL-125-NH₂ for photocatalytic NADH regeneration and gas-liquid-solid three-phase enzymatic CO₂ reduction, *Angew. Chem. Int. Ed.* 61 (2022), e202206283.
- [3] S.K. Kuk, R.K. Singh, D.H. Nam, R. Singh, J.-K. Lee, C.B. Park, Photoelectrochemical reduction of carbon dioxide to methanol through a highly efficient enzyme cascade, *Angew. Chem., Int. Ed.* 56 (2017) 3827–3832.
- [4] S. Zhang, J. Shi, Y. Sun, Y. Wu, Y. Zhang, Z. Cai, Y. Chen, C. You, P. Han, Z. Jiang, Artificial thylakoid for the coordinated photoenzymatic reduction of carbon dioxide, *ACS Catal.* 9 (2019) 3913–3925.
- [5] A. Rodriguez-Abetxuko, A. Reifs, D. Sánchez-deAlcázar, A. Belouqui, A versatile chemoenzymatic nanoreactor that mimics NAD(P)H oxidase for the in situ regeneration of cofactors, *Angew. Chem. Int. Ed.* 61 (2022), e202206926.
- [6] O. Bachar, M.M. Meirovich, Y. Zeibaq, O. Yehezkel, Protein-mediated biosynthesis of semiconductor nanocrystals for photocatalytic NAD(P)H regeneration and chiral amine production, *Angew. Chem., Int. Ed.* 61 (2022), e202202457.
- [7] Y. Tian, Y. Zhou, Y. Zong, J. Li, N. Yang, M. Zhang, Z. Guo, H. Song, Construction of functionally compartmental inorganic photocatalyst–enzyme system via imitating chloroplast for efficient photoreduction of CO₂ to formic acid, *ACS Appl. Mater. Interfaces* 12 (2020) 34795–34805.
- [8] C. Zhang, H. Zhang, J. Pi, L. Zhang, A. Kuhn, Bulk electrocatalytic NADH cofactor regeneration with bipolar electrochemistry, *Angew. Chem. Int. Ed.* 61 (2022), e202111804.
- [9] S.H. Lee, D.S. Choi, S.K. Kuk, C.B. Park, Photobiocatalysis: activating redox enzymes by direct or indirect transfer of photoinduced electrons, *Angew. Chem., Int. Ed.* 57 (2018) 7958–7985.
- [10] Y. Zhao, H. Liu, C. Wu, Z. Zhang, Q. Pan, F. Hu, R. Wang, P. Li, X. Huang, Z. Li, Fully conjugated two-dimensional sp²-carbon covalent organic frameworks as artificial photosystems with high efficiency, *Angew. Chem. Int. Ed.* 58 (2019) 5376–5381.
- [11] L. Zedler, P. Wintergerst, A.K. Mengele, C. Müller, C. Li, B. Dietzek-Ivanšić, S. Rau, Outpacing conventional nicotinamide hydrogenation catalysis by a strongly communicating heterodinuclear photocatalyst, *Nat. Commun.* 13 (2022) 2538.
- [12] J. Ryu, S.H. Lee, D.H. Nam, C.B. Park, Rational design and engineering of quantum-dot-sensitized TiO₂ nanotube arrays for artificial photosynthesis, *Adv. Mater.* 23 (2011) 1883–1888.
- [13] S.H. Lee, J. Ryu, D.H. Nam, C.B. Park, Photoenzymatic synthesis through sustainable NADH regeneration by SiO₂-supported quantum dots, *Chem. Commun.* 47 (2011) 4643–4645.
- [14] Z. Zhao, D. Zheng, M. Guo, J. Yu, S. Zhang, Z. Zhang, Y. Chen, Engineering olefin-linked covalent organic frameworks for photoenzymatic reduction of CO₂, *Angew. Chem., Int. Ed.* 61 (2022), e202200261.
- [15] X. Wang, H.H.P. Yiu, Heterogeneous catalysis mediated cofactor NADH regeneration for enzymatic reduction, *ACS Catal.* 6 (2016) 1880–1886.
- [16] Y. Wang, J. Sun, H. Zhang, Z. Zhao, W. Liu, Tetra(4-carboxyphenyl)porphyrin for efficient cofactor regeneration under visible light and its immobilization, *Catal. Sci. Technol.* 8 (2018) 2578–2587.
- [17] V. Ganesan, D. Sivanesan, S. Yoon, Correlation between the Structure and Catalytic Activity of [Cp*Rh(Substituted Bipyridine)] Complexes for NADH Regeneration, *Inorg. Chem.* 56 (2017) 1366–1374.
- [18] H.C. Lo, O. Buriez, J.B. Kerr, R.H. Fish, Regioselective reduction of NAD⁺ models with [Cp*Rh(bpy)H]⁺: structure–activity relationships and mechanistic aspects in the formation of the 1,4-NADH derivatives, *Angew. Chem. Int. Ed.* 38 (1999) 1429–1432.
- [19] S. Zhou, Y. Cai, J. Zhang, Y. Liu, L. Zhou, J. Lei, Au-loaded resorcinol–formaldehyde resin photocatalysts: hollow sphere structure design and localized surface plasmon resonance effect synergistically promote efficient nicotinamide adenine dinucleotide (NADH) regeneration, *ACS Sustain. Chem. Eng.* 10 (2022) 14464–14473.
- [20] T. Saba, J. Li, J.W.H. Burnett, R.F. Howe, P.N. Kechagiopoulos, X. Wang, NADH regeneration: a case study of Pt-catalyzed NAD⁺ reduction with H₂, *ACS Catal.* 11 (2021) 283–289.
- [21] T. Saba, J.W.H. Burnett, J. Li, X. Wang, J.A. Anderson, P.N. Kechagiopoulos, X. Wang, Assessing the environmental performance of NADH regeneration methods: a cleaner process using recyclable Pt/Fe₃O₄ and hydrogen, *Catal. Today* 339 (2020) 281–288.
- [22] Y. Wu, J. Shi, D. Li, S. Zhang, B. Gu, Q. Qiu, Y. Sun, Y. Zhang, Z. Cai, Z. Jiang, Synergy of electron transfer and electron utilization via metal–organic frameworks as an electron buffer tank for nicotinamide regeneration, *ACS Catal.* 10 (2020) 2894–2905.
- [23] W. Liu, W. Hu, L. Yang, J. Liu, Single cobalt atom anchored on carbon nitride with well-defined active sites for photo-enzyme catalysis, *Nano Energy* 73 (2020), 104750.
- [24] X. Li, Y. Cao, K. Luo, Y. Sun, J. Xiong, L. Wang, Z. Liu, J. Li, J. Ma, J. Ge, H. Xiao, R. N. Zare, Highly active enzyme–metal nanohybrids synthesized in protein–polymer conjugates, *Nat. Catal.* 2 (2019) 718–725.
- [25] F. Zhang, X. Li, Q. Zhao, G. Chen, Q. Zhang, High-performance In₂O₃@PANI core@shell architectures with ultralong charge carriers lifetime for photocatalytic degradation of gaseous 1,2-dichlorobenzene, *Appl. Catal. B: Environ.* 263 (2020), 118278.
- [26] X. Chen, H. Li, H. Wu, Y. Wu, Y. Shang, J. Pan, X. Xiong, Fabrication of TiO₂@PANI nanobelts with the enhanced absorption and photocatalytic performance under visible light, *Mater. Lett.* 172 (2016) 52–55.
- [27] T. Li, J.-D. Cui, L.-M. Gao, Y.-Z. Lin, R. Li, H. Xie, Y. Zhang, K. Li, Competitive self-assembly of PANI confined MoS₂ boosting the photocatalytic activity of the graphitic carbon nitride, *ACS Sustain. Chem. Eng.* 8 (2020) 13352–13361.
- [28] D.-D. Chen, X.-H. Yi, C. Zhao, H. Fu, P. Wang, C.-C. Wang, Polyaniline modified MIL-100(Fe) for enhanced photocatalytic Cr(VI) reduction and tetracycline degradation under white light, *Chemosphere* 245 (2020), 125659.
- [29] A. Shirmardi, M.A.M. Teridi, H.R. Azimi, W.J. Basirun, F. Jamali-Sheini, R. Yousefi, Enhanced photocatalytic performance of ZnSe/PANI nanocomposites for degradation of organic and inorganic pollutants, *Appl. Surf. Sci.* 462 (2018) 730–738.
- [30] B. Niu, Z. Xu, A stable Ta₃N₅@PANI core-shell photocatalyst: shell thickness effect, high-efficient photocatalytic performance and enhanced mechanism, *J. Catal.* 371 (2019) 175–184.
- [31] F. Chen, W. An, Y. Li, Y. Liang, W. Cui, Fabricating 3D porous PANI/TiO₂-graphene hydrogel for the enhanced UV-light photocatalytic degradation of BPA, *Appl. Surf. Sci.* 427 (2018) 123–132.
- [32] D. Yang, Y. Zhang, H. Zou, S. Zhang, Y. Wu, Z. Cai, J. Shi, Z. Jiang, Phosphorus quantum dots-facilitated enrichment of electrons on g-C₃N₄ hollow tubes for visible-light-driven nicotinamide adenine dinucleotide regeneration, *ACS Sustain. Chem. Eng.* 7 (2018) 285–295.
- [33] H. Fattahimoghaddam, T. Mahvelati-Shamsabadi, B.-K. Lee, Enhancement in photocatalytic H₂O₂ production over g-C₃N₄ nanostructures: a collaborative approach of nitrogen deficiency and supramolecular precursors, *ACS Sustain. Chem. Eng.* 9 (2021) 4520–4530.
- [34] L.J. Pan, L. Pu, Y. Shi, T. Sun, R. Zhang, Y.O. Zheng, Hydrothermal synthesis of polyaniline mesostructures, *Adv. Funct. Mater.* 16 (2006) 1279–1288.
- [35] X. Zhu, Z. Song, Z. Wang, W. Liu, B. Hong, J. Bao, C. Gao, S. Sun, Selective formation of interfacial bonding enables superior hydrogen production in organic–inorganic hybrid cocatalyzed photocatalysts, *Appl. Catal. B: Environ.* 274 (2020), 119010.
- [36] C. Janáky, N.R. de Tacconi, W. Chanmanee, K. Rajeshwar, Bringing conjugated polymers and oxide nanoarchitectures into intimate contact: light-induced electrodeposition of polypyrrole and polyaniline on nanoporous WO₃ or TiO₂ nanotube array, *J. Phys. Chem. C* 116 (2012) 19145–19155.
- [37] Y. Shiraishi, T. Takii, T. Hagi, S. Mori, Y. Kofuji, Y. Kitagawa, S. Tanaka, S. Ichikawa, T. Hirai, Resorcinol–formaldehyde resins as metal-free semiconductor photocatalysts for solar-to-hydrogen peroxide energy conversion, *Nat. Mater.* 18 (2019) 985–993.
- [38] H. Zengin, W. Zhou, J. Jin, R. Czerw, D.W. Smith Jr, L. Echegoyen, D.L. Carroll, S. H. Foulger, J. Ballato, Carbon nanotube doped polyaniline, *Adv. Mater.* 14 (2002) 1480–1483.
- [39] D. Chen, F. Zhang, W. Wang, Y. Yang, G. Qian, Synergistic effect of PANI and NiFe₂O₄ for photocatalytic hydrogen evolution under visible light, *Int. J. Hydrog. Energy* 43 (2018) 2121–2129.
- [40] J. Liu, Y. Liu, N. Liu, Y. Han, X. Zhang, H. Huang, Y. Lifshitz, S.-T. Lee, J. Zhong, Z. Kang, Metal-free efficient photocatalyst for stable visible water splitting via a two-electron pathway, *Science* 347 (2015) 970–974.
- [41] C.T.J. Ferguson, N. Huber, K. Landfester, K.A.I. Zhang, Dual-responsive photocatalytic polymer nanogels, *Angew. Chem. Int. Ed.* 58 (2019) 10567–10571.
- [42] J. Liu, M. Antonietti, Bio-inspired NADH regeneration by carbon nitride photocatalysis using diatom templates, *Energy Environ. Sci.* 6 (2013) 1486–1493.
- [43] Y. Maenaka, T. Suenobu, S. Fukuzumi, Efficient catalytic interconversion between NADH and NAD⁺ accompanied by generation and consumption of hydrogen with a water-soluble iridium complex at ambient pressure and temperature, *J. Am. Chem. Soc.* 134 (2012) 367–374.
- [44] M. Wang, X. Ren, M. Guo, J. Liu, H. Li, Q. Yang, Chemoselective NADH regeneration: the synergy Effect of TiO_x and Pt in NAD⁺ hydrogenation, *ACS Sustain. Chem. Eng.* 9 (2021) 6499–6506.
- [45] F. Zhang, X. Li, Q. Zhao, G. Chen, Q. Zhang, High-performance In₂O₃@PANI core@shell architectures with ultralong charge carriers lifetime for photocatalytic degradation of gaseous 1,2-dichlorobenzene, *Appl. Catal. B: Environ.* 263 (2020), 118278.
- [46] G. Fang, X. Li, X. Chen, Y. You, W. Dai, F. Qu, D. Tang, Z. Yan, Z-scheme Ag₃PO₄@polyaniline core-shell nanocomposite with high visible light photocatalytic performance for Microcystis aeruginosa inactivation, *Chem. Eng. J.* 427 (2022), 132005.